geosciences

MDPI

Article

Quantification of Coastal Change and Preliminary Sediment Budget Calculation Using SfM Photogrammetry and Archival Aerial Imagery

Rafael C. Carvalho [1,2,*] and Ruth Reef [1]

[1] School of Earth, Atmosphere and Environment, Monash University, Clayton, VIC 3800, Australia
[2] School of Earth, Atmospheric and Life Sciences, University of Wollongong, Wollongong, NSW 2500, Australia
* Correspondence: rafael.carvalho@monash.edu

Abstract: A preliminary sediment budget for the sandy shores flanking the entrance to Western Port, a large bay in Australia, was formulated using a comparison between two Digital Surface Models (DSMs) with a 30-year interval and auxiliary shoreline data. The 1977 DSM was generated from ten aerial photographs using Structure-from-Motion (SfM) photogrammetry. Assessment of its accuracy obtained an RMSE of 0.48 m with most of the independent points overpredicting or underpredicting elevations by less than 0.5 m following manual point cloud cleaning. This technique created a 7.5 km^2 surface with a Ground Sampling Distance of 34.3 cm between two coastal towns separated by a narrow channel. Comparison of the 1977 DSM to a second, light detection and ranging (LiDAR)-derived DSM from 2007 showed that a volume of ~200,000 m^3 of sediment (above Mean Sea Level) was deposited at Newhaven Beach on Phillip Island, while, during the same period, ~40,000 m^3 of sediment was lost from the mainland beaches of San Remo, on the eastern side of the channel. Shoreline positions extracted from aerial photographs taken in 1960 and a nautical chart published one century earlier indicate that the progradation experienced at Newhaven Beach has been possible due to provision of sediment via destabilisation of the vegetation covering the updrift Woolamai isthmus on the southeast coast of Phillip Island, whereas the retreat observed at San Remo Beach since 1960 can be attributed to the natural dynamics of the entrance, which appears to favour flood-dominance on the western side and ebb-dominance on the eastern side. While a more comprehensive balance of volumes entering and exiting the area would specifically benefit from volumetric assessments of the subaqueous part of the entrance, the general usefulness of quantifying coastal change using SfM and historical photographs is demonstrated.

Keywords: aerial photogrammetry; historical archive; LiDAR; balance of sediments; morphological change; sandy beaches

check for updates

Citation: Carvalho, R.C.; Reef, R. Quantification of Coastal Change and Preliminary Sediment Budget Calculation Using SfM Photogrammetry and Archival Aerial Imagery. *Geosciences* **2022**, *12*, 357. https://doi.org/10.3390/geosciences12100357

Academic Editors: Javier Leon, Luis Conti, Peter Feldens, Fabrizio Antonioli and Jesus Martinez-Frias

Received: 31 May 2022
Accepted: 19 September 2022
Published: 26 September 2022

1. Introduction

Beaches represent some of the most dynamic coastal landforms fringing approximately 40% of the world's coastline [1]. Quantification of the dynamic processes in these constantly changing environments is challenging [2,3], but is paramount for proper spatial planning, sustainable development and mitigation of climate change impacts [4,5].

Beach studies have long benefited from aerial photography as a means of recording change [2,6]. This aerial data source serves as a valuable archive of past landforms [7], which has been primarily used to evaluate 2D-projected horizontal displacements in shoreline position e.g., [5,8,9], while fewer studies have analysed 3D changes in sediment volume using photogrammetric principles, e.g., [10–12].

The gap in the application of the photogrammetric reconstruction technique for obtaining three-dimensional spatial information is attributed to the poor quality of historic photographs, low image overlap flight plans, scale variation among photographic datasets, relief displacement, computation of photo-coordinates and aerial triangulation on the

accuracy of measurements [13–18]. In addition to tide dependency, beach analyses often lack image texture and identifiable features to be used as ground control points [3,19].

Structure-from-Motion Multi-View Stereo, the topographic survey technique that has recently emerged from traditional photogrammetry and advances in computer vision [20,21], uses much more of the information contained within the imagery to aid the orientation process, unlocking large historical photogrammetric archives for morphological analyses [22]. This technique, referred to in this study as SfM photogrammetry [23], offers the potential to generate high accuracy dense point clouds at different spatial scales to restitute the three-dimensional geometry of surfaces and landforms [15,24,25] such as sandy beaches. Broad examples of coastal applications of SfM photogrammetry using historical aerial images include the works of Gomez et al. [26], Redweik et al. [27] and Ishiguro et al. [28]. However, studies quantifying the volumetric change of sandy coastlines are restricted to Carvalho et al. [19,29] and Grottoli et al. [30].

In this study, we apply SfM photogrammetry to a historical aerial imagery dataset collected in 1977 to quantify the volumetric change that occurred at the sandy shorelines flanking the entrance of Western Port, a bay in southeastern Australia. The historical digital surface model (DSM) was compared to a Light Detection and Ranging (LiDAR)-derived DSM acquired in 2007 to formulate a preliminary sediment budget for the area following an evaluation of the bundle adjustment (the process to estimate the 3D geometry, the camera poses and intrinsic parameters) and the quality of the historical DSM. This sediment budget approach creates a balance of volumes for sediments entering and leaving a selected coastal sector for management purposes [31–33]. Its formulation also benefited from shoreline positions extracted from aerial photographs taken in 1960 and a nautical chart published in the 1860s.

2. Coastal Setting

The study sites of San Remo and Newhaven are located on the southeastern side of Western Port (WP), Victoria, Australia (Figure 1). WP is a long (~50 km) and wide (~30 km) drowned embayment associated with the patterns of rifting and sedimentation experienced since the separation of the southern margin of the Australian and the Antarctic plates in the Mesozoic [34]. The bay has an unusual annular shape (ring-shaped configuration around French Island) and is bounded by pronounced topographic faulty scarps and a central uplifted block where two islands, Phillip and French, are located, a narrow horst to its west, volcanogenic-rich lithic sediments to its east, and early Tertiary basalts to the south [35].

The Eastern Entrance is the secondary connection of WP to the Bass Strait (the main one being the Western Entrance). The Eastern Entrance is about 1.5 km wide and sheltered from southwesterly waves by the granitic Cape Woolamai and the 500 m wide Woolamai isthmus between the cape and the main section of Phillip Island [36]. Sandy beaches intercalated by headlands and rock platforms are found on both sides of the Eastern Entrance, which funnels to approximately 450 m wide forming the scour channel known as 'The Narrows' between the towns of San Remo, on the mainland and Newhaven, on Phillip Island. This channel marks the division between two secondary-level sediment compartments used for management and planning purposes in Australia [37,38].

'The Narrows' reach more than 15 m below chart datum at its deepest point located about 400 m downstream from the bridge that connects both towns. The steep and narrow profile section of the channel generates current velocities that are significantly higher than elsewhere in WP [39]. Currents of 2.5 m/s are commonly observed during spring tides at the Eastern Entrance [40]. These are driven by semi-diurnal tides, the principal driving mechanism for water circulation with the lunar component M2 being strongly dominant and having an amplitude of 0.897 m at San Remo [41].

Water passing through the Eastern Entrance contributes to about 15% of the volume entering WP in any tidal cycle [40]. This inwards circulation causes some incursion of sand forming a small flood-tide delta to the north of the bridge [42], which led Marsden [43] and Marsden et al. [35] to infer a flood-dominant circulation and sediment transport through the entrance. However, uncertainty remains, as other studies [41,44,45] indicate an ebb-

dominant circulation pattern [39]. This has been corroborated by the existence of a sandy ebb-tide delta and sandy beaches mainly observed downstream of the bridge, suggesting that marine sands from offshore sources and weathered Pleistocene aeolianites are not transported in large amounts inwards.

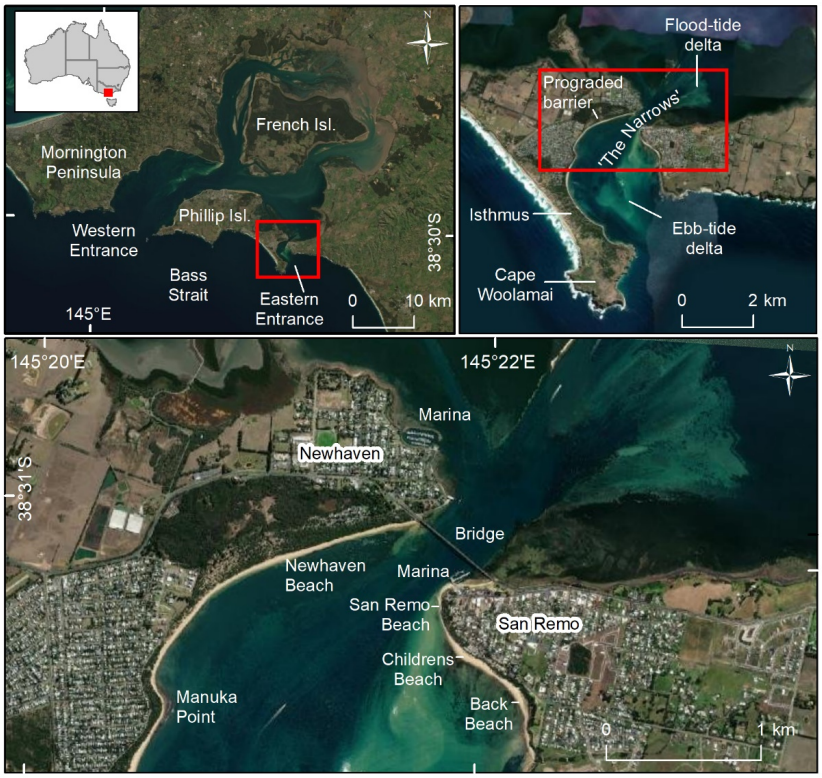

Figure 1. Study sites of San Remo and Newhaven located on the Eastern Entrance of Western Port, Victoria. A rocky seawall runs along the entire length of San Remo Beach and Childrens Beach. Important features described in the text are labelled. Basemap imagery from ArcGIS Online.

Detectable changes in the configuration of 'The Narrows' were observed previously during a survey conducted in 1963 for the construction of a new bridge connecting both sides of the channel [42]. This new bridge, which opened in 1969, replaced the old and smaller bridge that once existed to the west of the San Remo marina.

Instability of cliffs and significant erosion of the once continuous strip of sand affected the beaches on the eastern side of the channel in the past decades. This led to the construction of a continuous 830 m long rocky seawall to the south of the San Remo marina running along the entire length of San Remo Beach and Childrens Beach, which became very narrow and in parts, completely awash at high tide [46]. On the Newhaven side of the entrance, a 1.5 km long by 200 m wide prograded barrier exists to the west of the bridge. This barrier is composed of series of low ridges developed since the 1840s [47].

3. Materials and Methods

We applied SfM analysis to aerial photographs acquired in 1977 specifically for traditional photogrammetry. Pix4Dmapper v.4.7.5 (Lausanne, Switzerland) was used to assist bundle adjustment and georeferencing of the 1977 DSM and orthomosaic for a part of the Eastern Entrance of Western Port. Topographic LiDAR points captured in 2007 were processed and used to generate a LiDAR-derived DSM for volumetric comparisons, and to georeference and calculate the accuracy of the 1977 model. Auxiliary aerial photographs and a historical nautical chart provided important information for formulation of the preliminary sediment budget for the study area.

3.1. Data

Ten high resolution scanned analogue aerial photographs (approximately 50 Mb each) in digital format (.tiff) were used to generate the historical model. These black and white photographs were obtained in March 1977 at a scale of 1:10,000. The photographs (film number 3188) were obtained with an RC8 camera at an approximate flight height of 5000 feet from the ground during three non-parallel flight runs (15, 16 and 17). Photographs in each run had an overlap of approximately 65% with no sidelap between images. Each photograph had a footprint of approximately 2400 m × 2400 m.

Despite the availability of more recent aerial images (e.g., 1984 and 1989) for the entrance, only the 1977 images were suitable for SfM photogrammetry due to their high quality (reduced blur, darkness and haze), high level of overlapping [15,25,26] and the recommended scale (1:10,000 or larger) for topographic mapping [48]. A batch cropping process in ImageJ 1.53 k [49] was used to remove the black frame around the photographs prior to SfM processing.

Topographic LiDAR data surveys were carried out between 20 April–22 July 2007 with an Optech ALTM3100EA sensor mounted on an aircraft. The sensor collected X, Y, Z and intensity data for first and last returns by bouncing a pulse (footprint size of 0.2 m) from the aircraft to the surface. Five LAS files (classification Level 2 and ICSM accuracy Level 3 format), organised in 2 × 2 km tiles, were provided by the Victorian Department of Environment, Land, Water and Planning (DELWP). Reported horizontal and vertical accuracies for the LiDAR files (RMSE 68% Conf.) were 0.35 m and 0.1 m, respectively.

ArcMap v10.8.1 (Redlands, CA, USA) was used to process the LAS files into point shapefiles. Any return values were used during the conversion of the LAS files to bare ground (class 2) following ASPRS [50] specifications. Once processed, the points were used to create a Triangular Irregular Network (TIN), which was then converted to a DSM raster (pixel size of 1 m). Selected LiDAR points were also used as ground control points (GCPs) during the SfM processing of the 1977 images and as independent point for accuracy assessments. These points were carefully selected at locations where none or minimal change occurred between 1977 and 2007, such as roads, sidewalks and driveways.

3.2. SfM Photogrammetry Processing

The input camera model was not defined prior to processing, which relied solely on the software's self-calibration procedure. Processing of the 1977 model was initially conducted with arbitrary coordinates (no scale, orientation and absolute position information) due to the lack of geolocation information in scanned photographs. The initial processing was set to full image scale, aerial grid pair matching, automatic targeted number of keypoints, default calibration method and camera parameter optimisation. Point cloud densification used multiscale half size images (scale used to speed up processing recommended for blurry/low texture images) to compute additional 3D points for every eighth pixel of the original image (optimal), with a minimum of three matches per 3D point. A medium resolution (default) 3D textured mesh was also created during the process.

An arbitrary DSM was generated using noise filtering for altitude correction, default surface smoothing, and Inverse Distance Weighting interpolation. An orthomosaic was also generated as part of this process. These preliminary products (DSM and orthomosaic) allowed a visual reconnaissance of the model domain, identification and selection of points used as GCPs and in the accuracy assessment.

After this initial processing, a georeferenced model was created with GCPs a posteriori [7,22] technique. This followed the same initial processing, point cloud, mesh, DSM and orthomosaic configurations used before. The georeferenced model used a total of 15 GCPs spread through the model (Figure 2), with assigned accuracy position of 0.5 m in each (X, Y and Z) domain. The final products had the same projected coordinate system (GDA 94 Zone 55S) and vertical Datum (AHD09) as the LiDAR data.

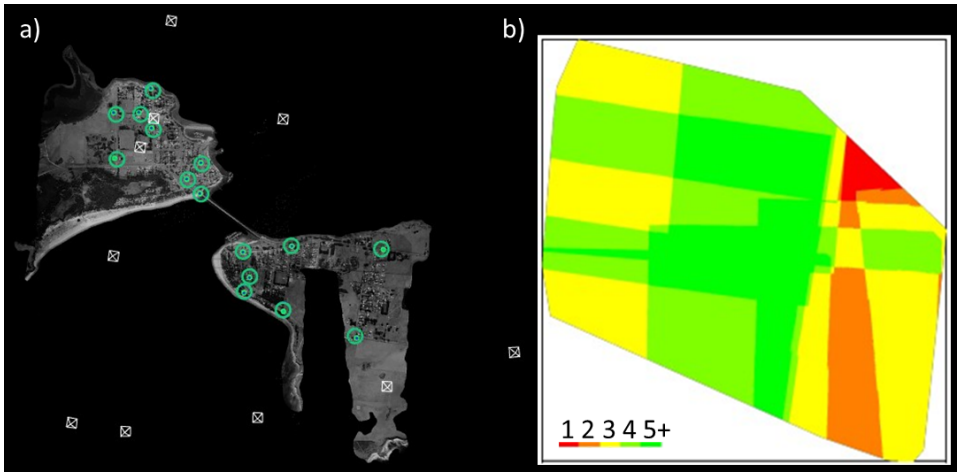

Figure 2. Areas covered by triangle meshes for the historical model (**a**) and colour-coded number of overlapping images (**b**). White crosses represent photographic locations while green circles show individual GCPs added to model.

Manual cleaning of the point cloud removed spikes and artefacts in the 1977 model. These were most common on tree canopies and over homogeneous low texture areas, such as paved and unsealed roads, pasture, water bodies and parts of the beach. After point cloud cleaning, final products (3D textured mesh, DSM and orthomosaic) were created. Visualisation of the 3D textured mesh is available at https://skfb.ly/o9T8R (accessed on 30 May 2022).

3.3. Accuracy Assessments

A total of 51 independent LiDAR points were used in the accuracy assessments of the 1977 DSM [21,51] (Figure 3). The elevation of these points was compared with those extracted from the final DSM.

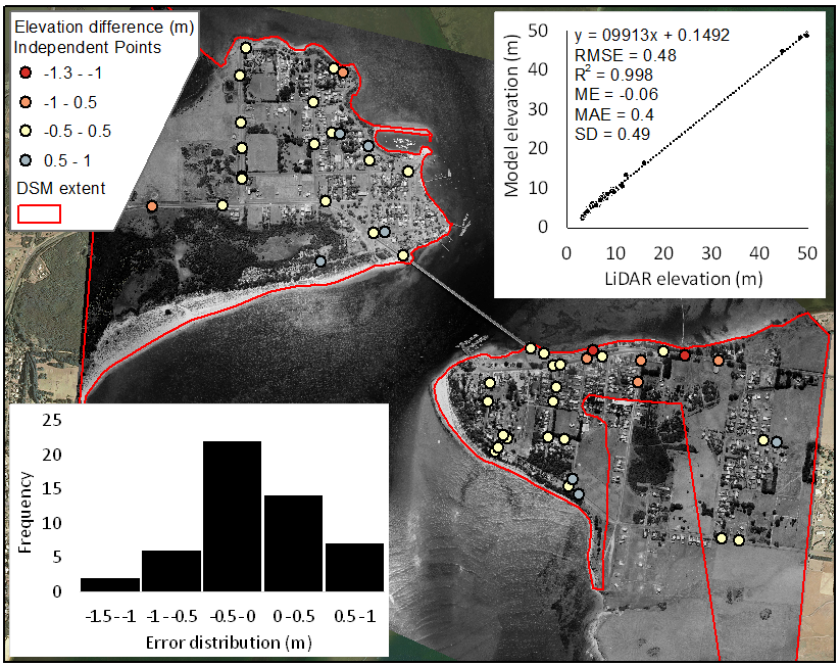

Figure 3. The 1977 DSM extent and orthomosaic. Coloured points show the elevation difference (m) for each of the 51 points used in the accuracy assessment between the 2007 LiDAR data and the 1977 DSM. Negative values (cold colours) indicate elevations higher than LiDAR, while positive values (hot colours) denote elevations lower than LiDAR. The frequency distribution of errors and model evaluation parameters are included as insets.

3.4. Volumetric Comparison

A Digital Elevation Model (DEM) of Difference (DoD) was calculated by subtracting the historical DSM from the 2007 LiDAR-derived DSM. This initially covered the whole area extent of the 1977 DSM (Figure 3) and allowed a broad visual comparison of the two models.

Specific volumetric comparisons were made to beach areas to the south of the bridge on both sides of the channel and calculated above 0 m AHD (Australian Height Datum, equivalent to Mean Sea Level). These masked areas mostly covered the beach face to avoid urbanised and vegetated areas that were subject to change.

The inherent uncertainty of volumetric analyses was calculated based on a spatially variable threshold of the two DSMs [52,53]. This threshold (0.49 m) accounted for the standard deviation of the vertical accuracy of the LiDAR and the RMSE of the 1977 model. The volumetric uncertainty was then calculated using the area experiencing change (number of pixels) that had absolute values larger than the threshold multiplied by the uncertainty cube (pixel area x the threshold) [19,29].

3.5. Auxiliary Data Used in Sediment Budget

Apart from the aerial photographs used in the SfM photogrammetry process, another seven aerial images were georeferenced to provide information for the formulation of the sediment budget of the entrance. Two of these images were captured in February 1977 at a scale of 1:10,000, and five were taken in March 1960 at 1:15,840 scale (Figure 4).

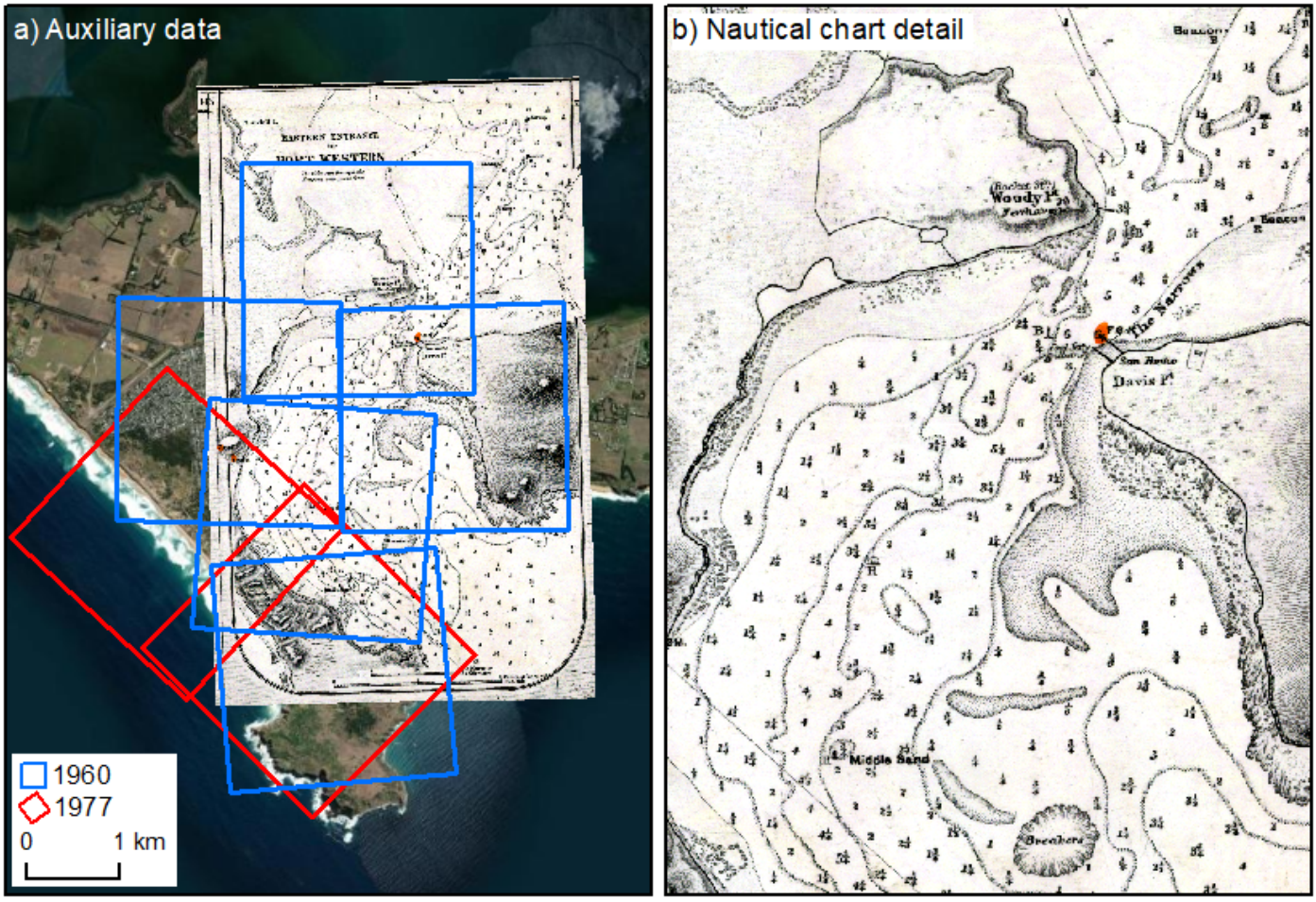

Figure 4. Footprint of the auxiliary georeferenced aerial photographs taken in 1960 and 1977 and nautical chart insert published in 1867 used in the formulation of the sediment budget (**a**). Zoomed-in area showing chart details between San Remo and Newhaven (**b**). Chart publicly available at the State Library Victoria.

An insert of the historical nautical chart "Port Western", published at the Admiralty in 1867, showing the Eastern Entrance was also used as an important source of early information. This nautical chart surveyed by H. L. Cox is part of a set of charts of Victoria's coastline published in the 1850s and 1860s marked by significant improvements in terms of cartographic technique in relation to the charts made by early explorers [54,55].

Georeferencing of the nautical chart insert used five GCPs and had an RMSE of 7 m, while GCPs for each aerial photograph ranged between 6 and 11 with RMSEs of less than 2 m. Shoreline information was digitised from these data sources using ArcMap v10.8.1 at 1:10,000 scale.

4. Results and Discussion

4.1. SfM and Model Accuracy

Approximately 1,800,000 3D densified points with an average density of 0.06 point per m^3 were generated from the ten photographs. The spatial extent of 7.5 km^2 and Ground Sampling Distance (GSD) of 34.3 cm, reflected the RC8 camera parameters, the flight height (5000 feet) and the overlap of images. An overall georeferencing RMSE of 0.68 m was obtained from the use of 15 GCPs, with mean RMSEs of 0.77 m, 0.93 m and 0.34 m for the X, Y and Z domains, respectively. The 1977 model had a median of 12,232 keypoints per image, 2717 matches per calibrated image, and 19.73% of camera optimisation.

A very strong relationship (R^2 = 0.998) was obtained between the LiDAR points and the ones extracted from the 1977 DSM at localities identified as being unlikely to change (Figure 3). The RMSE of the 1977 model was only 0.48 m, the mean error (ME) was −0.06 m, the standard deviation of errors (SD) was 0.49 m, and the mean absolute error (MAE) was 0.4 m. The frequency distribution of errors reflected the model evaluation parameters with most independent points overpredicting (n = 22) or underpredicting (n = 14) LiDAR elevations by less than 0.5 m.

4.2. DSM Comparison

The 1977 historical model showed elevations comparable to the 2007 LiDAR DSM (Figure 5). Elevations in the 1977 model ranged from −1.3 to 67.6 m AHD (Figure 5a), whereas the processed LiDAR ranged from −0.9 to 65.2 m AHD for the same area (Figure 5b). In general, observed urban changes were related to development such as the construction of new dwellings, changes to the Newhaven marina breakwater, and growth and removal of trees (Figure 5c). Changes to the shoreline between 1977 and 2007 occurred particularly along the Newhaven Beach from the southern side the bridge all the way to Manuka Point (Figure 1), and on the opposite side of the Eastern Entrance between the San Remo and Back beaches (Figure 5f).

At San Remo, erosion occurred from the south of the marina to Childrens Beach (Figure 5g–i) and deposition was observed further to the south along Back Beach, which was devoid of sand in 1977. The erosion removed a volume of 60,996 ± 10,621 m^3 (Figure 5i), while the accretion of sand added a volume of approximately 20,977 ± 5574 m^3 to Back Beach (Figure 5j). At Newhaven Beach, the shoreline prograded up to 65 m between 1977 and 2007, gaining almost 60,000 m^2 of sediment along the 1.5 km of beach length from the bridge to Manuka Point (Figure 5k). This equated to an accretion of 199,890 ± 29,830 m^3 (6700 m^3/y) of sand above MSL.

Oblique views of the coast showing major changes along both sides of the channel can be observed in Figure 6. Erosion at San Remo Beach (Figure 6a,b) contrasts with accretion at Back Beach (Figure 6c,d) and Newhaven Beach (Figure 6e,f) between 1977 and 2007. Elevation profiles (A-A') extracted from the middle of Newhaven Beach exemplify the experienced progradation since 1977 (Figure 6g).

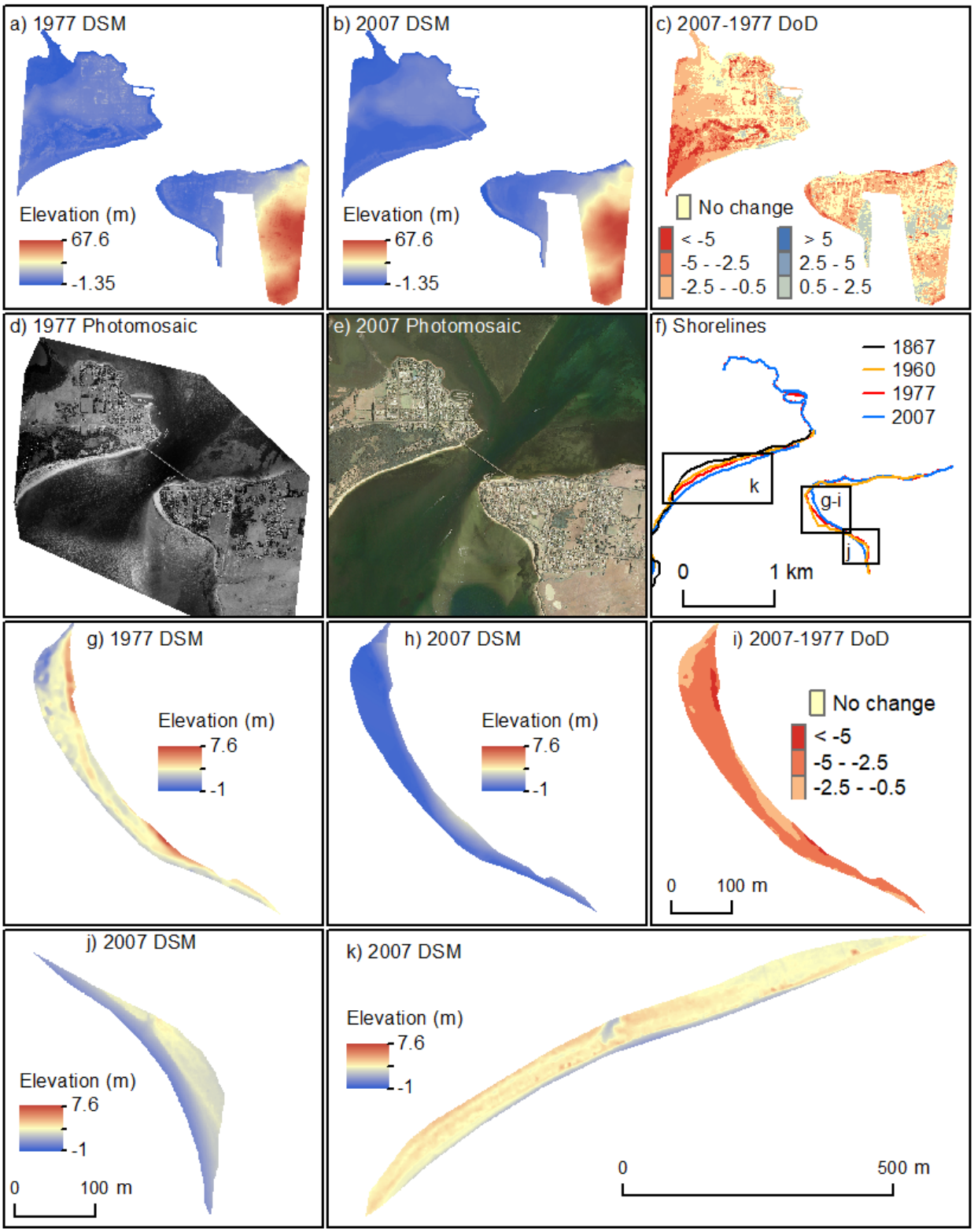

Figure 5. DSMs (**a**,**b**), DoD (**c**), photomosaics (**d**,**e**) and digitised shoreline (**f**) comparison. Specific DSMs (**g**,**h**) and DoD (**i**) show erosion observed at San Remo-Childrens beaches, whereas 2007 DSMs show subaerial deposition (accretion) experienced at Back Beach (**j**) and Newhaven Beach (**k**). Negative values (red) in DoDs indicate areas of erosion, whereas positive values (blue) indicate areas where deposition occurred. An absolute value of 0.5 m based on the RMSE was used to represent areas of no change (yellow). Auxiliary digitised shorelines are added for comparison (**f**). The 1977 DSM (**a**) and photomosaic (**d**) are available as Supplementary Materials.

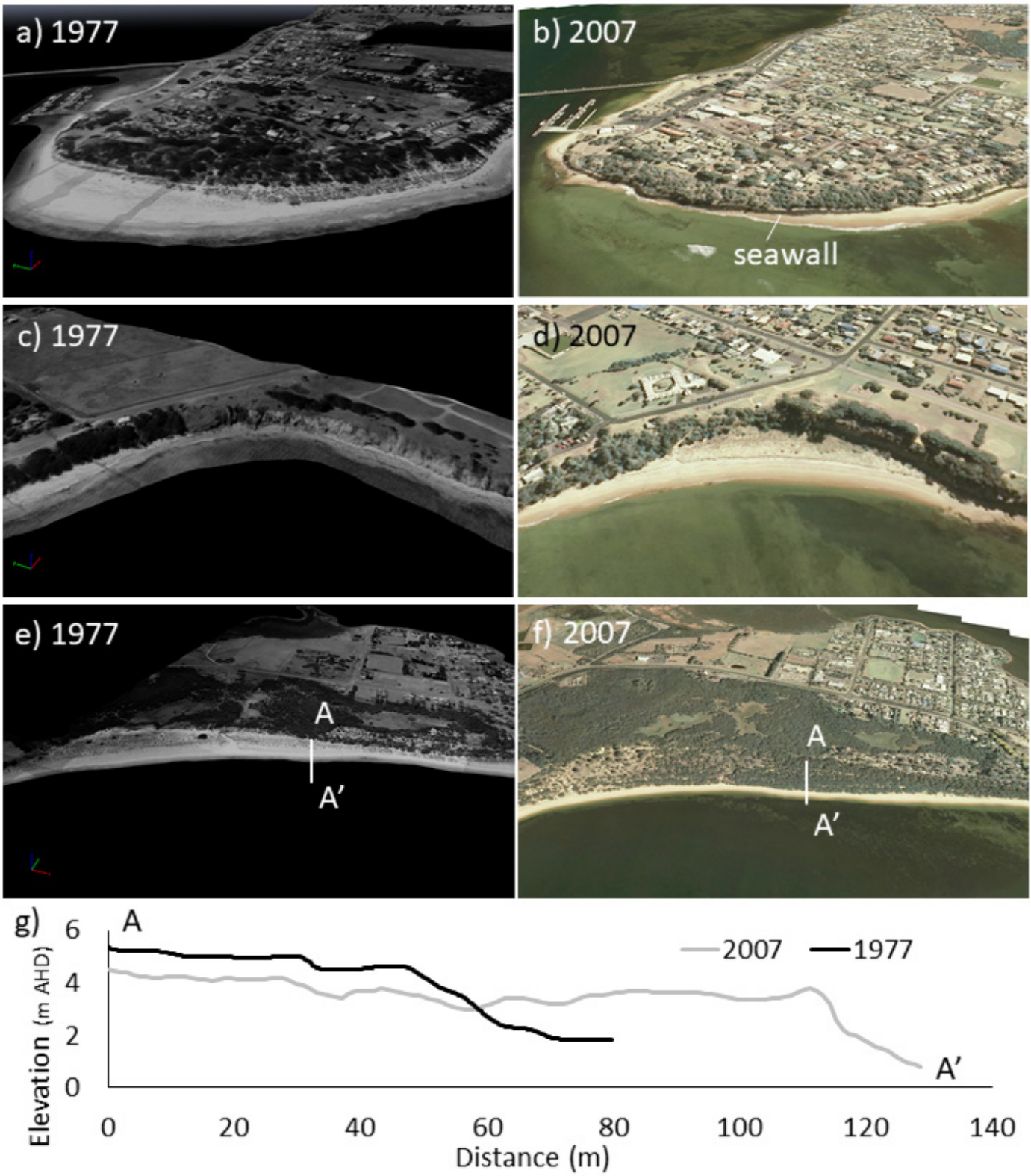

Figure 6. Oblique views in 1977 (**left**) and 2007 (**right**) at San Remo Beach (**a**,**b**), Back Beach (**c**,**d**) and Newhaven Beach (**e**,**f**) showing the eroding vs. depositional contrasting behaviour experienced along the shoreline on the eastern side of the channel, and the accretion experienced on the western side. Elevation profiles over time extracted from a section of the Newhaven Beach shows approximately 50 m of progradation since 1977 (**g**).

4.3. Shoreline Change Prior to 1977

It appears that the progradation experienced at Newhaven Beach has been an ongoing process for approximately 150 years. This has been evidenced by the shoreline position digitised from the 1867 nautical chart (Figure 5f). This chart shows part of the Newhaven Beach shoreline located up to about 100 m behind its 1977 position and reveals the existence of rocks through most of its entire 1.5 km length (Figure 4b). This progradation history is corroborated by a set of aerial photographs taken in 1960 that shows the shoreline up to 38 m landwards of its 1977 position.

On the other side of the channel, the shoreline position in 1960 shows that more sand existed to the south of the San Remo marina (all the way to Childrens Beach) prior to 1977 (Figure 5f), whereas further south at Back Beach, the shoreline position remained roughly the same over the 17-year period. Due to cartographic limitations and possible omissions, no shoreline position can be extracted from the 1867 chart on the eastern side of the channel.

4.4. The Use of SfM on Photographic Archive

This study re-emphasises the usefulness of SfM photogrammetry to generate historical elevation models to quantify beachface volumetric changes, and to create seamless photomosaics, which can be used in traditional shoreline analysis [19,29,30]. It can also produce unlimited perspectives of the landscape, which provide qualitative ways of understanding how the coast evolved [19,27,29].

The 1977 DSM created in this study was of good quality as determined by the comparison against independent points (Figure 3). The accuracy measurements and the spatial and frequency distribution of errors were slightly better than the ones obtained in previous studies using photographs taken at similar scale [19,29,30]. These performance indicators also demonstrated the normality of the error distribution and their non-directionality [56–58].

The quality of the results, however, was achieved after extensive manual labour to clean the point cloud and remove undesirable surfaces created by the low overlapping of images and low-visual homogenous areas not providing enough information for optimal camera calibration. Future developments of the technique should incorporate different automated attempts to filter and clean point clouds such as the ones performed by Grottoli et al. [30], or the ones that exploit the spectral properties of the photographs [59–61].

Improvements can also be made if the camera model parameters were defined in Pix4Dmapper, as self-calibration optimisation of the bundle adjustment within the software results in non-linear systematic errors [62,63]. However, insertion of focal length, principal points, radial and tangential distortions, for instance, is not an easy task given the lack of information regarding the different camera lenses that could have been used.

4.5. A Preliminary Sediment Budget for the Eastern Entrance

A positive balance of approximately 160,000 m^3 of sand is obtained between 1977 and 2007 when the volume eroded from San Remo Beach (~61,000 m^3) is subtracted from the gains experienced at Back Beach (~21,000 m^3) and Newhaven Beach (~200,000 m^3). Considering uncertainties, this gain can be as high as 256,220 m^3 and as low as 113,846 m^3. This large input of material mostly deposited on the shores of Newhaven Beach is closely related to the vegetation changes that occurred at the Woolamai isthmus since the 19th century.

The introduction of rabbits following European colonisation disturbed the vegetation cover and disestablished the transgressive dune fields that form the isthmus [64]. The dunes have an estimated volume of 12,500,000 m^3 of sand [36], and their mobility led to large amounts of sand being supplied from Woolamai Beach to the Cleveland Bight Beach, which prograded up to 80 m from 1867 to 1960. The available sand was transported via longshore currents supplying material for the downdrift shores all the way to Newhaven Beach (Figure 7a).

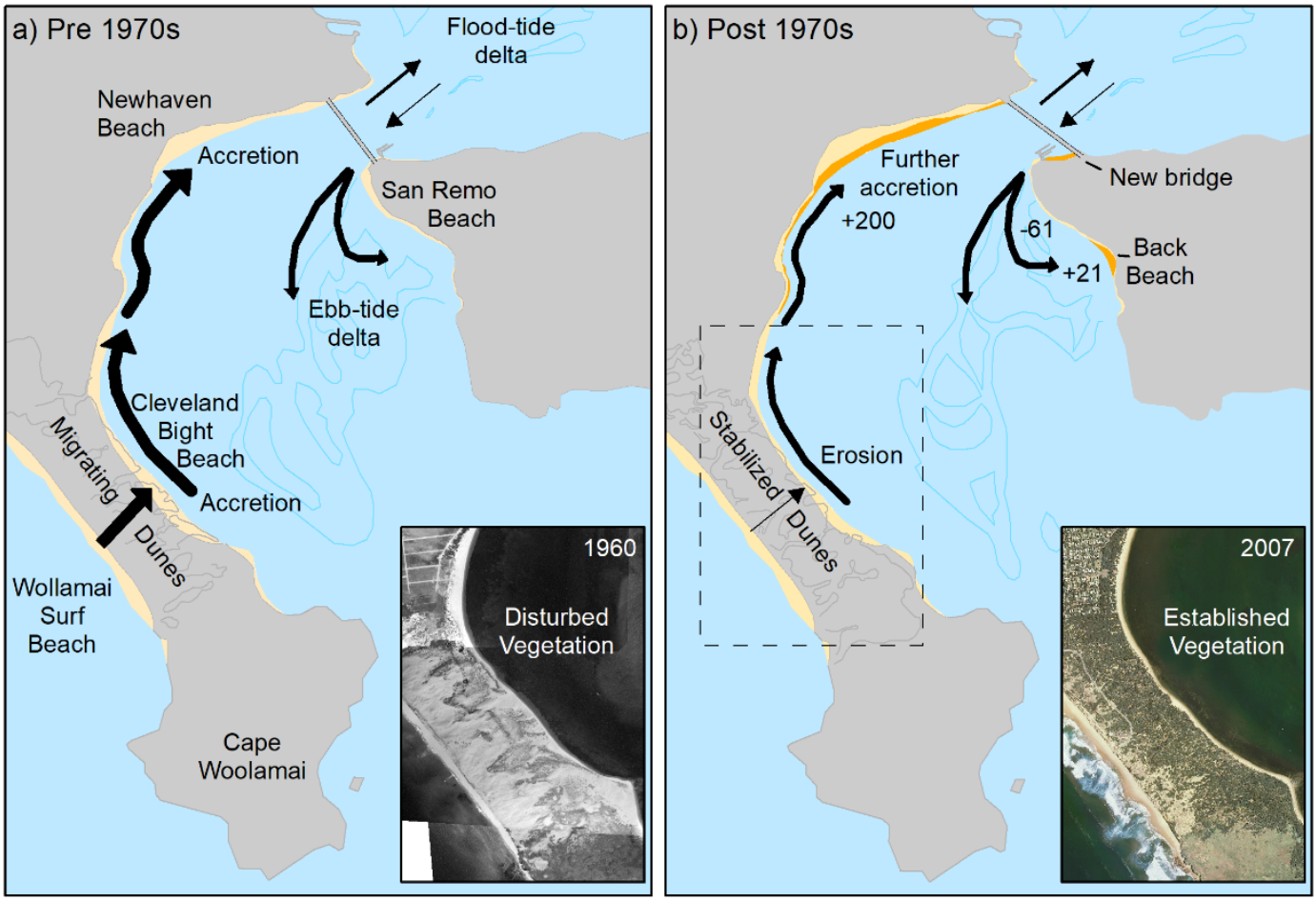

Figure 7. Preliminary sediment budget scheme for the Eastern Entrance before (**a**) and after (**b**) stabilisation of mobile dunes in the Woolamai isthmus. Arrow thickness indicates inferred volume of sediment transported. Accretion experienced from 1977 to 2007 is represented in orange, while numbers represent approximate volumes (in 1000 m^3). Aerial photograph inserts show disturbed and established vegetation following Marram grass planting in the dashed area.

A further progradation of up to 35 m was experienced at Newhaven Beach during the 1960–1977 period. The progradation continued after 1977 at the expense of the Cleveland Bight Beach, which started to erode following the planting of marram grass in the late 1970s and gradual stabilisation of the migrating dunes [64] (Figure 7b).

Between 1977 and 2007, a maximum recession of 35 m occurred at Cleveland Bight Beach. Despite being almost half of the maximum distance (65 m) experienced at Newhaven during the same period, the steepness of the eroded beach/dune system must have provided a volume close to the 200,000 m^3 of sand added to the much flatter Newhaven Beach.

At San Remo, a subaerial volume of 40,000 m^3 was removed from the system between 1977 and 2007. This was preceded by aa visual estimation of approximately 25,000 m^3 removed between 1960 and 1977. Some of this material was trapped to the east of the marina following the construction of the new bridge in 1969. However, given the ebb-dominance on the eastern side of the channel, it is plausible to assume that most of this material was incorporated to the ever-changing ebb-tide delta. Sand wave configuration forming the ebb-tide delta alternates erosion and accretion along the eastern shores of the channel [36].

Uncertainties remain in relation to the volumetric changes experienced at both ebb and flood-tide deltas. However, given the vast quantities of mud-size particles surrounding the small flood-tide delta [42], minimum volumes of sand are expected to be transported below the bridge during ebb tides, unless significant recirculation occurs. Refinements to

this preliminary scheme should include subaqueous calculation using the available nautical charts and bathymetry for the area [32,65]. This can be done even without additional fieldwork by just comparing soundings from historical sources to contemporary charts and available airborne data such as marine LiDAR.

5. Conclusions

This study demonstrates how sediment budgets can benefit from historical DSMs created using SfM photogrammetry applied to archival aerial photographs. We constructed a preliminary budget for the Eastern Entrance of Western Port, Australia, that allows estimates of the surplus of sediment deposited on the beach flanking the shores of Newhaven and the deficit of material at San Remo, on the opposite side of the channel, to be made.

Aerial images collected in 1977 at 1:10,000 scale were used to create a DSM, which was compared to a 2007 DSM generated from LiDAR returns. Fifteen bare ground LiDAR points at minimum disturbed or unaltered areas were used to georeference the 1977 model during the initial phase of the SfM process. A Ground Sampling Distance of 34.3 cm was obtained for this 1977 model. The accuracy measurements and the spatial and distribution of errors against 51 independent points demonstrated the good quality (R^2 = 0.998) of the final DSM after point cloud cleaning. An RMSE, SD and MAE of less than 50 cm were obtained with only 15 independent points either under or overpredicting results above this elevation threshold.

Quantification of volumetric changes along the two sides of the Eastern Entrance was calculated between 1977 and 2007. The 2007–1977 DoD showed that Newhaven Beach accreted approximately 200,000 m^3 during the 30-year period, while on the eastern side of the entrance, San Remo Beach lost about 61,000 m^3 and Back Beach gained 21,000 m^3. Additional information from aerial photographs taken in 1960 and 1977 and a historical nautical chart published in 1867 provided important information for the formulation of the budget. These auxiliary sources of data indicated that the large input of material deposited on the shores of Newhaven Beach is closely related to the vegetation changes that have occurred at the Woolamai isthmus since the 19th century, and that an estimated amount of approximately 25,000 m^3 was removed from San Remo Beach between 1960 and 1977.

Following European colonisation, destabilisation of the vegetation cover made the transgressive dunes of the Woolamai isthmus mobile and large amounts of sand were transported to the Eastern Entrance. This has provided sediments for the shoreline progradation experienced along the western side of the channel. After gradual stabilisation of the migrating dunes in the late 1970s, the shores of Newhaven continued to accrete, but this time at the expenses of the updrift beaches which started to erode. At the San Remo side of the channel, a negative balance of approximately 65,000 m^3 was estimated since 1960 (40,000 m^3 from 1977 to 2007 plus 25,000 m^3 from 1960 to 1977). Fate for this volume of sand is yet to be determined. However, the ebb-dominance conditions on the eastern side of the channel suggests that most of this material was incorporated to the ebb-tidal delta. Future assessments to the volumetric changes experienced in the subaqueous part of the entrance should refine the preliminary budget presented in this study.

Supplementary Materials: The following supporting information (The 1977 DSM and Photomosaic) can be downloaded at: https://www.mdpi.com/article/10.3390/geosciences12100357/s1.

Author Contributions: Conceptualisation, R.C.C.; methodology, R.C.C.; software, R.C.C.; validation, R.C.C.; formal analysis, R.C.C.; investigation, R.C.C.; resources, R.C.C.; data curation, R.C.C.; writing—original draft preparation, R.C.C.; writing—review and editing, R.C.C. and R.R.; visualisation, R.C.C.; supervision, R.R.; project administration, R.C.C.; funding acquisition, R.R. All authors have read and agreed to the published version of the manuscript.

Funding: This study was funded by the Australian Research Council Project DP180103444.

Data Availability Statement: Data supporting reported results can be obtained from the corresponding author. Visualisation of the 3D textured mesh is available at https://skfb.ly/o9T8R (accessed on 30 May 2022).

Acknowledgments: The authors would like to thank the Victorian Department of Environment, Land, Water and Planning for the provision of aerial photographs and LiDAR data. We also thank the two anonymous reviewers for their feedback and suggestions, which improved the manuscript.

Conflicts of Interest: The authors declare no conflict of interest.

References

1. Bird, E.C.F. *Coastal Geomorphology: An Introduction*; John Wiley & Sons Ltd.: Chichester, West Sussex, UK, 2008.
2. Baily, B.; Nowell, D. Techniques for Monitoring Coastal Change: A Review and Case Study. *Ocean Coast. Manag.* **1996**, *32*, 85–95. [CrossRef]
3. Mills, J.P.; Buckley, S.J.; Mitchell, H.L.; Clarke, P.J.; Edwards, S.J. A Geomatics Data Integration Technique for Coastal Change Monitoring. *Earth Surf. Process. Landf.* **2005**, *30*, 651–664. [CrossRef]
4. Luijendijk, A.; Hagenaars, G.; Ranasinghe, R.; Baart, F.; Donchyts, G.; Aarninkhof, S. The State of the World's Beaches. *Sci. Rep.* **2018**, *8*, 6641. [CrossRef]
5. Stafford, D.B.; Langfeld, J. Air Photo Survey of Coastal Erosion. *Photogramm. Eng.* **1971**, *37*, 565–575.
6. Thieler, E.R.; Danforth, W.W. Historical Shoreline Mapping (I): Improving Techniques and Reducing Positioning Errors. *J. Coast. Res.* **1994**, *10*, 549–563.
7. Nebiker, S.; Lack, N.; Deuber, M. Building Change Detection from Historical Aerial Photographs Using Dense Image Matching and Object-Based Image Analysis. *Remote Sens.* **2014**, *6*, 8310. [CrossRef]
8. Amrouni, O.; Hzami, A.; Heggy, E. Photogrammetric Assessment of Shoreline Retreat in North Africa: Anthropogenic and Natural Drivers. *ISPRS J. Photogramm. Remote Sens.* **2019**, *157*, 73–92. [CrossRef]
9. Dolan, R.; Hayden, B.; Heywood, J. A New Photogrammetric Method for Determining Shoreline Erosion. *Coast. Eng.* **1978**, *2*, 21–39. [CrossRef]
10. Doyle, T.B.; Short, A.D.; Ruggiero, P.; Woodroffe, C.D. Interdecadal Foredune Changes Along the Southeast Australian Coastline: 1942–2014. *J. Mar. Sci. Eng.* **2019**, *7*, 177. [CrossRef]
11. Hanslow, D.J. Beach Erosion Trend Measurement: A Comparison of Trend Indicators. *J. Coast. Res.* **2007**, *50*, 588–593.
12. Hapke, C.; Richmond, B. Monitoring Beach Morphology Changes Using Small-Format Aerial Photography and Digital Softcopy Photogrammetry. *Environ. Geosci.* **2000**, *7*, 32–37. [CrossRef]
13. Baily, B.; Collier, P.; Farres, P.; Inkpen, R.; Pearson, A. Comparative Assessment of Analytical and Digital Photogrammetric Methods in the Construction of Dems of Geomorphological Forms. *Earth Surf. Process. Landf.* **2003**, *28*, 307–320. [CrossRef]
14. Chandler, J. Effective Application of Automated Digital Photogrammetry for Geomorphological Research. *Earth Surf. Process. Landf.* **1999**, *24*, 51–63. [CrossRef]
15. Fonstad, M.A.; Dietrich, J.T.; Courville, B.C.; Jensen, J.L.; Carbonneau, P.E. Topographic Structure from Motion: A New Development in Photogrammetric Measurement. *Earth Surf. Process. Landf.* **2019**, *38*, 421–430. [CrossRef]
16. Grip, W.M.; Grip, R.W.; Morrison, R.D. Application of Aerial Photography and Photogrammetry in Environmental Forensic Investigations. *J. Environ. Forensics* **2000**, *1*, 121–129. [CrossRef]
17. Moore, L.J. Shoreline Mapping Techniques. *J. Coast. Res.* **2000**, *16*, 111–124.
18. Schenk, T. *Introduction to Photogrammetry*; The Ohio State University: Columbus, OH, USA, 2005; Volume 106.
19. Carvalho, R.C.; Allan, B.; Kennedy, D.M.; Leach, C.; O'Brien, S.; Ierodiaconou, D. Quantifying Decadal Volumetric Changes Along Sandy Beaches Using Improved Historical Aerial Photographic Models and Contemporary Data. *Earth Surf. Process. Landf.* **2021**, *46*, 1882–1897. [CrossRef]
20. James, M.R.; Robson, S. Straightforward Reconstruction of 3d Surfaces and Topography with a Camera: Accuracy and Geoscience Application. *J. Geophys. Res. Earth Surf.* **2012**, *117*, 1–17. [CrossRef]
21. Smith, M.W.; Carrivick, J.L.; Quincey, D.J. Structure from Motion Photogrammetry in Physical Geography. *Prog. Phys. Geogr.* **2016**, *40*, 247–275. [CrossRef]
22. Bakker, M.; Lane, S.N. Archival Photogrammetric Analysis of River-Floodplain Systems Using Structure from Motion (Sfm) Methods. *Earth Surf. Process. Landf.* **2017**, *42*, 1274–1286. [CrossRef]
23. James, M.R.; Chandler, J.H.; Eltner, A.; Fraser, C.; Miller, P.E.; Mills, J.P.; Noble, T.; Robson, S.; Lane, S.N. Guidelines on the Use of Structure-from-Motion Photogrammetry in Geomorphic Research. *Earth Surf. Process. Landf.* **2019**, *44*, 2081–2084. [CrossRef]
24. Carrivick, J.L.; Smith, M.W.; Quincey, D.J. *Structure from Motion in the Geosciences*; John Wiley & Sons: West Sussex, UK, 2016.
25. Westoby, M.J.; Brasington, J.; Glasser, N.F.; Hambrey, M.J.; Reynolds, J.M. Structure-from-Motion' Photogrammetry: A Low-Cost, Effective Tool for Geoscience Applications. *Geomorphology* **2012**, *179*, 300–314. [CrossRef]
26. Gomez, C.; Hayakawa, Y.; Obanawa, H. A Study of Japanese Landscapes Using Structure from Motion Derived Dsms and Dems Based on Historical Aerial Photographs: New Opportunities for Vegetation Monitoring and Diachronic Geomorphology. *Geomorphology* **2015**, *242*, 11–20. [CrossRef]
27. Redweik, P.; Garzón, V.; sá Pereira, T. Recovery of Stereo Aerial Coverage from 1934 and 1938 into the Digital Era. *Photogramm. Rec.* **2016**, *31*, 9–28. [CrossRef]
28. Ishiguro, S.; Yamano, H.; Oguma, H. Evaluation of Dsms Generated from Multi-Temporal Aerial Photographs Using Emerging Structure from Motion–Multi-View Stereo Technology. *Geomorphology* **2016**, *268*, 64–71. [CrossRef]

29. Carvalho, R.C.; Kennedy, D.M.; Niyazi, Y.; Leach, C.; Konlechner, T.M.; Ierodiaconou, D. Structure-from-Motion Photogrammetric Analysis of Historical Aerial Photography: Determining Beach Volumetric Change over Decadal Scales. *Earth Surf. Process. Landf.* **2020**, *45*, 2540–2555. [CrossRef]
30. Grottoli, E.; Biausque, M.; Rogers, D.; Jackson, D.W.T.; Cooper, J.A.G. Structure-from-Motion-Derived Digital Surface Models from Historical Aerial Photographs: A New 3d Application for Coastal Dune Monitoring. *Remote Sens.* **2021**, *13*, 95. [CrossRef]
31. Carvalho, R.C.; Woodroffe, C.D. The Sediment Budget as a Management Tool: The Shoalhaven Coastal Compartment, Southeastern Nsw, Australia. In Proceedings of the 23rd NSW Coastal Conference, Ulladulla, NSW, Australia, 11–14 November 2014.
32. Carvalho, R.C.; Woodroffe, C.D. Sediment Budget of a River-Fed Wave-Dominated Coastal Compartment. *Mar. Geol.* **2011**, *441*, 106617. [CrossRef]
33. Rosati, J.D. Concepts in Sediment Budgets. *J. Coast. Res.* **2005**, *21*, 307–322. [CrossRef]
34. Veevers, J.J.; McElhinny, M.W. The Separation of Australia from Other Continents. *Earth Sci. Rev.* **1976**, *12*, 139–143. [CrossRef]
35. Marsden, M.A.H.; Mallett, C.W.; Donaldson, A.K. Geological and Physical Setting, Sediments and Environments, Western Port, Victoria. *Mar. Geol.* **1979**, *30*, 11–46. [CrossRef]
36. Short, A.D. *Australian Coastal Systems: Beaches, Barriers and Sediment Compartments*; Springer Nature: Cham, Switzerland, 2020; Volume 32.
37. McPherson, A.; Hazelwood, M.; Moore, D.; Owen, K.; Nichol, S.; Howard, F. *The Australian Coastal Sediment Compartments Project: Methodology and Product Development*; Geoscience: Canberra, Australia, 2015.
38. Thom, B.G.; Eliot, I.; Eliot, M.; Harvey, N.; Rissik, D.; Sharples, C.; Short, A.D.; Woodroffe, C.D. National Sediment Compartment Framework for Australian Coastal Management. *Ocean Coast. Manag.* **2018**, *154*, 103–120. [CrossRef]
39. Harris, J.E.; Hinwood, J.B.; Marsden, M.A.H.; Sternberg, R.W. Water Movements, Sediment Transport and Deposition, Western Port, Victoria. *Mar. Geol.* **1979**, *30*, 131–161. [CrossRef]
40. Hinwood, J.B. *Westernport Bay—Tidal Data 1969*; Paper GFDL 32; Monash University: Clayton, OH, USA, 1970.
41. Hinwood, J.B.; Jones, J.C.E. Hydrodynamic Data for Western Port, Victoria. *Mar. Geol.* **1979**, *30*, 47–63. [CrossRef]
42. Marsden, M.A.H.; Mallett, C.W. Quaternary Evolution, Morphology, and Sediment Distribution, Westernport Bay, Victoria. *Proc. R. Soc. Vic.* **1975**, *87*, 107–138.
43. Marsden, M.A.H. Circulation Patterns from Seabed-Drifter Studies, Western Port and Inner Bass Strait, Australia. *Mar. Geol.* **1979**, *30*, 85–99. [CrossRef]
44. Harris, J.E.; Robinson, J.B. Circulation in Western Port, Victoria, as Deduced from Salinity and Reactive-Silica Distributions. *Mar. Geol.* **1979**, *30*, 101–116. [CrossRef]
45. Hinwood, J.B. Hydrodynamic and Transport Models of Western Port, Victoria. *Mar. Geol.* **1979**, *30*, 117–130. [CrossRef]
46. Short, A.D. *Beaches of the Victorian Coast & Port Phillip Bay: A Guide to Their Nature, Characteristics, Surf and Safety*; Sydney University Press: Sydney, Australia, 1996.
47. Bird, E.C.F. Historical Changes on Sandy Shorelines in Victoria. *Proc. R. Soc. Vic.* **1980**, *91*, 17–32.
48. Avery, T.E.; Berlin, G.L. *Interpretation of Aerial Photographs*; Burgess Publishing Co.: Minneapolis, MN, USA, 1962.
49. Schneider, C.A.; Rasband, W.S.; Eliceiri, K.W. Nih Image to Imagej: 25 Years of Image Analysis. *Nat. Methods* **2012**, *9*, 671–675. [CrossRef]
50. ASPRS. *Las Specification 1.4—R14*; American Society for Photogrammetry and Remote Sensing: MD, USA, 2011.
51. Eltner, A.; Kaiser, A.; Castillo, C.; Rock, G.; Neugirg, F.; Abellán, A. Image-Based Surface Reconstruction in Geomorphometry—Merits, Limits and Developments. *Earth Surf. Dyn.* **2016**, *4*, 359–389. [CrossRef]
52. Brasington, J.; Langham, J.; Rumsby, B. Methodological sensitivity of morphometric estimates of coarse fluvial sediment transport. *Geomorphology* **2003**, *53*, 299–316. [CrossRef]
53. Wheaton, J.M.; Brasington, J.; Darby, S.E.; Sear, D.A. Accounting for uncertainty in DEMs from repeat topographic surveys: Improved sediment budgets. *Earth Surf. Process. Landf.* **2010**, *35*, 136–156. [CrossRef]
54. Carvalho, R.C.; Kennedy DMYoung, M.; Leach CIerodiaconou, D. Relevance of Historical Nautical Charts in Sediment Dynamic Assessments On a High Energy Temperate Shelf. *Cont. Shelf Res.* **2021**, *230*, 104555. [CrossRef]
55. Eccleston, G.C. *The Early Charting of Victoria's Coastline: With Comments on Victoria's Maritime Boundaries*; Australian and New Zealand Map Society: Parkes, Australia, 2012.
56. Höhle, J.; Höhle, M. Accuracy Assessment of Digital Elevation Models by Means of Robust Statistical Methods. *ISPRS J. Photogramm. Remote Sens.* **2009**, *64*, 398–406. [CrossRef]
57. Smith, M.W.; Vericat, D. From Experimental Plots to Experimental Landscapes: Topography, Erosion and Deposition in Sub-Humid Badlands from Structure-from-Motion Photogrammetry. *Earth Surf. Process. Landf.* **2015**, *40*, 1656–1671. [CrossRef]
58. Willmott, C.J.; Matsuura, K. Advantages of the Mean Absolute Error (Mae) over the Root Mean Square Error (Rmse) in Assessing Average Model Performance. *Climat. Res.* **2005**, *30*, 79–82. [CrossRef]
59. Callow, J.N.; May, S.M.; Leopold, M. Drone Photogrammetry and Kmeans Point Cloud Filtering to Create High Resolution Topographic and Inundation Models of Coastal Sediment Archives. *Earth Surf. Process. Landf.* **2018**, *43*, 2603–2615. [CrossRef]
60. Chehata, N.; David, N.; Bretar, F. Lidar Data Classification Using Hierarchical K-Means Clustering. Presented at the XXI ISPRS Congress Beijing 2008, Beijing, China, 3–11 July 2008.
61. Montealegre, A.L.; Lamelas, M.T.; de la Riva, J. A Comparison of Open-Source Lidar Filtering Algorithms in a Mediterranean Forest Environment. *IEEE J. Sel. Top. Appl. Earth Obs. Remote Sens.* **2015**, *8*, 4072–4085. [CrossRef]

62. James, M.R.; Robson, S. Mitigating systematic error in topographic models derived from UAV and ground-based image network. *Earth Surf. Process. Landf.* **2010**, *39*, 1413–1420. [CrossRef]
63. Wackrow, R.; Chandler, J.H. A convergent image configuration for DEM extraction that minimises the systematic effects caused by an inaccurate lens model. *Photogramm. Rec.* **2008**, *23*, 6–18. [CrossRef]
64. Bird, E.C.F. *The Coast of Victoria: The Shaping of Scenery*; Melbourne University Press: Melbourne, Australia, 1993.
65. Carvalho, R.C.; Woodroffe, C.D. Modifications to the Shoalhaven Estuary and the Coastal Sediment Budget over the Past 40 Years. In Proceedings of the Australasian Coasts & Ports 2017: Working with Nature, Cairns, Australia, 21–23 June 2017.